Biomechanics and Modeling in Mechanobiology, manuscript No.
(will be inserted by the editor)

Anterior mitral leaflet curvature in the beating ovine heart

A case study using videoflouroscopic markers and subdivision surfaces

S. Goktepe · W. Bothe · J-P. E. Kvitting · J.C. Swanson · N.B. Ingels · D.C. Miller · E. Kuhl

Received: date / Accepted: date

Abstract The implantation of annuloplasty rings is a common surgical treatment targeted to re-establish mitral valve competence in patients with mitral regurgitation. It is hypothesized that annuloplasty ring implantation influences leaflet curvature, which in turn may considerably impair repair durability. This research is driven by the vision to design repair devices that optimize leaflet curvature to reduce valvular stress. In pursuit of this goal, the objective of this manuscript is to quantify leaflet curvature in ovine models with and without annuloplasty ring using *in vivo* animal data from videofluoroscopic marker analysis. We represent the surface of the anterior mitral leaflet based on 23 radiopaque markers using subdivision surfaces techniques. Quartic box spline functions are applied to determine leaflet curvature on overlapping subdivision patches. We illustrate the virtual reconstruction of the leaflet surface for both interpolating and approximating algorithms. Different scalar-valued metrics are introduced to quantify leaflet curvature in the beating heart using the approximating subdivision scheme. To explore the impact of annuloplasty ring implantation, we analyze ring-induced curvature changes at characteristic instances throughout the cardiac cycle. The presented results demonstrate that the fully automated subdivision surface procedure can successfully reconstruct a smooth representation of the anterior mitral valve from a limited number of markers at a high temporal resolution of approximately 60 frames per minute.

Keywords Mitral valve, mitral regurgitation, annuloplasty ring, curvature, subdivision surfaces, continuitiy

S. Goktepe
Department of Mechanical Engineering, Stanford, CA-94305, USA, E-mail: goktepe@stanford.de

W. Bothe, J-P. E.Kvitting, J.C. Swanson, D.C. Miller
Department of Cardiothoracic Surgery, Stanford, CA 94305, USA, E-mail: wbothe/kvitting/ swansjul/dcm@stanford.edu

N.B. Ingels
Laboratory of Cardiovascular Physiology and Biophysics, Palo Alto Medical Foundation, Palo Alto, CA 94304, USA and Department of Cardiothoracic Surgery, Stanford, CA 94305, USA, E-mail: ingels@stanford.edu

E. Kuhl
Departments of Mechanical Engineering, Bioengineering, and Cardiothoracic Surgery, Stanford, CA-94305, USA, E-mail: kuhl@stanford.de

1 Motivation

Mitral regurgitation is a progressive, valvular disorder that affects approximately 4 million people in the United States with 250,000 new cases occurring each year. Annually, more than 300,000 people worldwide, 44,000 in the US alone, undergo open heart surgery for mitral valve treatment [2, 7]. The mitral valve is a bicuspid heart valve consisting of two leaflets, anterior and posterior, surrounded by the mitral valve annulus. A normal mitral valve allows unidirectional blood flow from the left atrium into the left ventricle during diastole and prevents back flow during systole. In mitral regurgitation, the valve fails to close properly and blood leaks backward with each heartbeat, lowering pumping efficiency.

The most common surgical approach to repair a leaking valve is to bring the leaflets closer together by implanting an annuloplasty ring around the mitral valve annulus. Annuloplasty rings come in different shapes, oval versus dog-bone shaped, flat versus saddle-contoured, may be constructed from a rigid or flexible material, and are available in an assortment of sizes. One example is the Edwards GeoForm® ring illustrated in Fig-

ure 1. Specifically designed to restore leaflet coaptation and treat mitral regurgitation, it has a characteristic dogbone shape to significantly reduce the valve septal-lateral dimensions [1, 29], shown as the middle vertical dimension in the top view of Figure 1. Choosing the optimal ring type and size depends primarily on the surgeon's experience and personal preference. It is hypothesized that both ring shape and stiffness considerably influence leaflet and annular dynamics.

Elevated leaflet stresses have been postulated to cause long-term repair failure. Unfortuantely, it is impossible to measure leaflet stresses in the beating heart. Continuum mechanics based descriptions of leaflet dynamics, solved with finite element techniques, offer the potential to predict stress profiles *in vivo*. These approaches, however, require a precise understanding of the material properties, boundary conditions, and forces of the entire mitral valve apparatus [13, 15, 19, 20, 30]. Early finite element based stress analyses indicate that the GeoForm® ring might significantly reduce maximum principal leaflet stresses [29]. The effect of annuloplasty rings on leaflet stresses has only recently been quantified *in vivo* [1], but the complex interplay between ring form and function is not fully understood to date.

Rather than determining leaflet material properties, evaluating leaflet equilibrium, and then quantifying leaflet stress [14], we propose a more straightforward approach based on a direct analysis of leaflet kinematics [11, 25]. We hypothesize that mitral leaflet curvature immediately influences leaflet stresses, and thus has a direct impact on mitral valve function [26]. In the literature, leaflet curvature has been accessed using three-dimensional echocardiography [24]. The resulting images of the mitral leaflet were manually segmented, manually merged, and approximated with smooth splines. Based on a least squares fit, a parameterized surface representation was generated to determine Gaussian curvature in ovine models with and without annuloplasty rings [23].

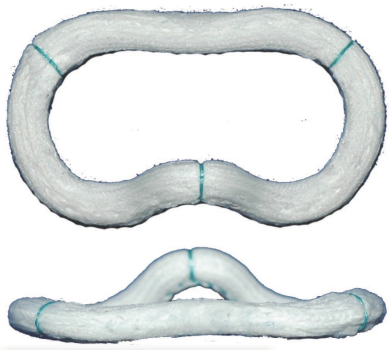

Fig. 1 Annuloplasty rings are a common surgical approach to repair a leaking valve. The GeoForm® ring has a characteristic dogbone shape with a significantly elevated posterior segment to bring the leaflets closer together and prevent back flow.

The present manuscript presents an alternative approach to quantify leaflet curvature based on a high resolution videofluoroscopic marker analysis evaluated with a novel subdivision surface algorithm. We illustrate the features of the proposed approach in terms of two data sets, one with the GeoForm® ring implanted and one with the ring released in the same ovine heart. To define leaflet curvature in terms of the acquired marker coordinates, we adopt a subdivision surface approach. The concept of subdivision surfaces was introduced in the late 1970s to address the challenge of generating smooth free-form surfaces of arbitrary topologies [3,9]. Rather than assembling individual patches of tensor product splines, subdivision surface algorithms generate a spline patch as the limit of a repeated uniform knot intersection. Initially developed in geometry and applied mathematics [17,21,22,31], subdivision surface algorithms are currently receiving a broad attention in computer graphics [27, 28]. Due to their inherent $\mathcal{C}^1$-continuity, the structural mechanics community has recently recognized subdivision surfaces as a new paradigm to characterize higher order derivatives in advanced shell theories [4–6]. In this manuscript, we apply the generic idea of subdivision, to create a parameterized surface representation of the anterior mitral leaflet. We utilize local overlapping patches of subdivision triangles to determine the global second order curvature field with the help of quartic box splines [4]. In addition to the Gaussian curvature field discussed in the literature [24], we also visualize the mean and principal curvatures, and compare and discuss the different curvature representations.

The manuscript is organized as follows: Section 2 briefly summarizes our experimental technique to determine four-dimensional leaflet marker coordinates. Section 3 compares interpolating and approximating schemes and introduces the concept of subdivision surfaces. In Section 4, we illustrate the curvature computation and discuss different scalar-valued curvature measures. The features of the proposed approach are demonstrated in Section 5 by means of a characteristic leaflet curvature analysis in an ovine model with and without annuloplasty ring. Potential applications of the proposed approach are discussed in Section 6.

2 Mitral leaflet coordinates

An adult Dorsett-hybrid male sheep was premedicated with ketamine, anesthetized with sodium thiopental, intubated, and mechanically ventilated with inhalational isoflurane. A left thoracotomy was performed and the

heart was suspended in a pericardial cradle. On cardiopulmonary bypass, a total of 23 radiopaque tantalum markers were sewn to the following sites: seven on the anterior mitral annulus, seven on the mitral leaflet edge, and nine on the leaflet belly, see Fig. 2. To identify maximum leaflet opening, an addition marker was sewn on the central edge of the middle scallop of the posterior mitral leaflet. Each tantalum marker weighed 3.2mg and had an inner and outer diameter of 0.6mm and 1.1mm, respectively. After marker placement, a true-sized GeoForm® annuloplasty ring was implanted with a specifically-designed technique such that it could be released in the catheterization laboratory while the heart is beating [1]. After ring implantation, the left atrium was closed, the animal was weaned from cardiopulmonary bypass, and a micromanometer transducer was placed in the left ventricle through the left atrium. The animal was then transferred to the experimental catheterization laboratory. It was placed in the

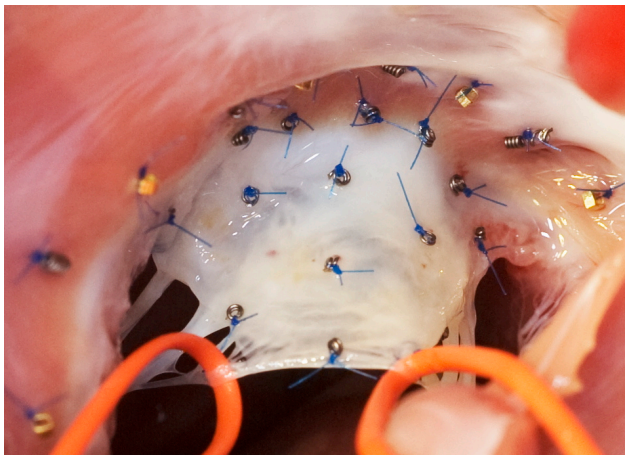

Fig. 2 Intraoperative photograph showing some of the twenty-three tantalum markers sewn to the mitral valve. Seven markers are sewn on the anterior mitral annulus, seven on the mitral leaflet edge, and nine on the leaflet belly.

right lateral decubitus position for acquisition of data under open-chest condition, see Fig. 3. For left ventricular and atrial pressure measurements, a micromanometer pressure transducer and a calibrated catheter were place in the left ventricle and left atrium, respectively. Videofluoroscopic images at 60 frames per second were acquired of all radiopaque markers using a biplane videofluoroscopy system with the heart in normal sinus rhythm and ventilation transiently arrested at end expiration.

First, images were acquired with the ring attached to the annulus. Then the ring was released [1]. Ring release was verified fluoroscopically and another data acquisition was performed under baseline conditions to serve as control. Marker coordinates from each of the biplane views were then merged to yield the 3D coordinates of each marker centroid in each frame using semi-automated image processing and digitization software developed in our laboratory [8,18]. Left ventricular and atrial pressure were digitally recorded simultaneously during marker data acquisition and synchronized with the marker coordinates. The above described procedure generates four-dimensional marker coordinates for all 23 markers. In the following section we compare different techniques to represent the leaflet surface in terms of these marker coordinates.

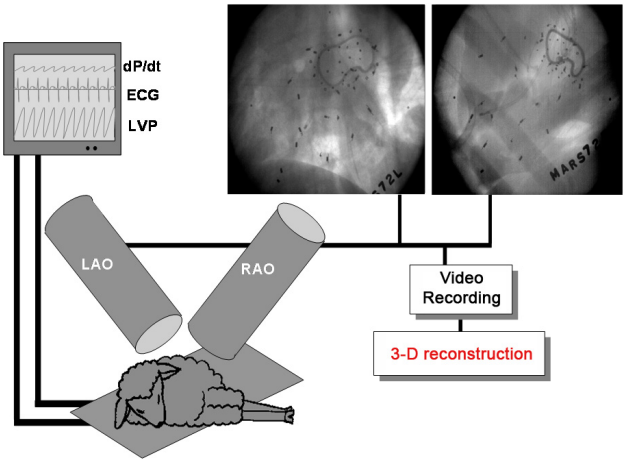

Fig. 3 Data acquisition in the catheterization laboratory. The sheep is imaged under open-chest conditions using biplane videofluoroscopy at 60 frames per second. Four-dimensional marker coordinates are generated by merging the time sequences from both cameras.

3 Surface representation

Subdivision surface algorithms are a powerful tool to mathematically define arbitrary free-form surfaces based on a given set of control points. A subdivision algorithm consists of two ingredients, a topological split algorithm defining how the connectivity of the control mesh is refined, and a geometric refinement algorithm introducing the nodal coordinates of the new refinement level. The refinement of a coarse mesh is carried out by quadrisecting triangular elements in the coarser mesh. During quadrisection, each edge connecting two nodes in the coarse mesh is divided into two edges through insertion of newly generated nodes. Depending on the underlying geometric refinement algorithm, surface representation algorithms can be divided into two classes, interpolating and approximating schemes. In what follows, we compare the geometric refinement rules for

these two schemes. Thereby we restrict ourselves to surfaces which consist of trianglar faces only.

3.1 Interpolating schemes

Interpolating schemes preserve the nodal positions of the coarser mesh upon refinement [31]. This implies that nodes of the original control mesh and all recursively generated nodes will always lie exactly on the limit surface. Accordingly, interpolating schemes are free of approximation errors, however, their limit surfaces do not have a well-defined curvature. Fig. 4 illustrates a typical sequence of interpolating surfaces. The k+1-th level of refinement is generated by maintaining the coordinates of old nodes $\boldsymbol{x}_0^k$ of the k-th level,

$$\boldsymbol{x}_0^{k+1} = \boldsymbol{x}_0^k \tag{1}$$

and by introducing new nodes $\boldsymbol{x}_I^{k+1}$ on its edges. The positions of the newly inserted nodes are calculated by averaging the weighted nodal positions of the unrefined mesh.

$$\boldsymbol{x}_I^{k+1} = \tfrac{1}{8}\,[\,3\,\boldsymbol{x}_0^k + \boldsymbol{x}_{I-1}^k + 3\,\boldsymbol{x}_I^k + \boldsymbol{x}_{I+1}^k\,] \tag{2}$$

Only the four nodes of two triangles that share the edge of interest contribute the averaging equation (2). The refinement mask for the newly inserted nodes in Fig.6 (right) demonstrates the distribution of the weighting factors 1 8 and 3 8 assigned to the four nodes [17]. Since the subdivision process itself is linear, the resulting limit surface is nothing but a linear combination of fundamental solutions of the subdivision process.

3.2 Approximating schemes

Approximating schemes introduce an entirely new set of nodal positions for each refinement step. Accordingly, nodes of the original control mesh may no longer be

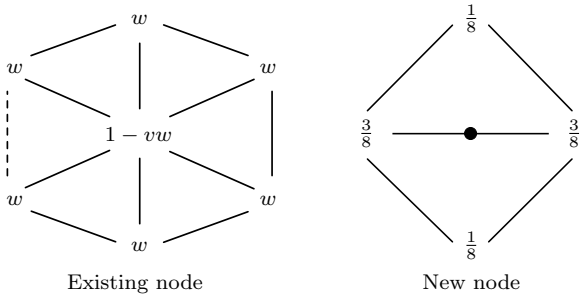

Fig. 6 Refinement mask for different algorithms. Existing nodes are maintained for the interpolating scheme and refined for the approximating scheme, left. New nodes are calculated by averaging the weighted nodal positions of the unrefined mesh for both schemes, right.

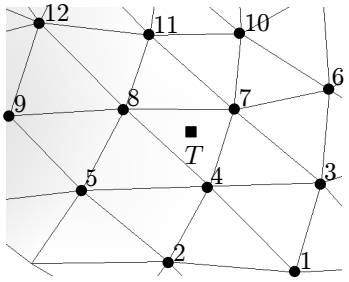

Fig. 7 Regular patch with twelve nodes used for the curvature interpolation on triangle T.

part of the limit surface. Approximating subdivision algorithms are thus associated with an approximation error. In contrast to interpolating schemes, approximating schemes can generate $\mathcal{C}^1$-continuous limit surfaces with a well-defined curvature provided that elements with irregular vertices are recursively refined. A typical approximating series of subdivision surfaces is illustrated in Fig. 5. The coordinates of the $k+1$-th refinement step are computed as weighted averages of the nodal coordinates of the k-th refinement level. The old nodes $\boldsymbol{x}_0^k$ are assigned new coordinates $\boldsymbol{x}_0^{k+1}$ according the the following formula,

$$\boldsymbol{x}_0^{k+1} = [\,1 - vw\,]\,\boldsymbol{x}_0^k + w \sum_{i=1}^{v} \boldsymbol{x}_I^k \tag{3}$$

while the newly generated nodes $\boldsymbol{x}_I^{k+1}$ associated with the edges of the k-th refinement are computed similarly to the interpolating scheme.

$$\boldsymbol{x}_I^{k+1} = \tfrac{1}{8}\,[\,3\,\boldsymbol{x}_0^k + \boldsymbol{x}_{I-1}^k + 3\,\boldsymbol{x}_I^k + \boldsymbol{x}_{I+1}^k\,] \tag{4}$$

In equation (3), w is a weight function and v denotes the valence of the node under consideration [17], i.e., the number of edges connected to it, see Fig. 6 (left). In a perfectly regular triangular mesh, the valence of all inner nodes is $v = 6$, but usually a few nodes of the original control mesh are irregular with a valence of $v = 6$. All newly generated nodes, however, have a valence of $v = 6$ by construction.

Remark 1 (Special treatment at surface boundaries) Special care needs to be taken at kinematic boundaries where the subdivision algorithm needs to be modified. In our examples, we use the method of artificial nodes which generates an artificial mirror image of the original mesh along the boundary and applies the standard subdivision rule as illustrated in [4].

Remark 2 (Error of the approximation) While the interpolating scheme always keeps the marker positions on the subdivision surface, the approximating scheme inherently introduces an approximation error. This approximation error can be characterized through different error norms such as the root mean square error

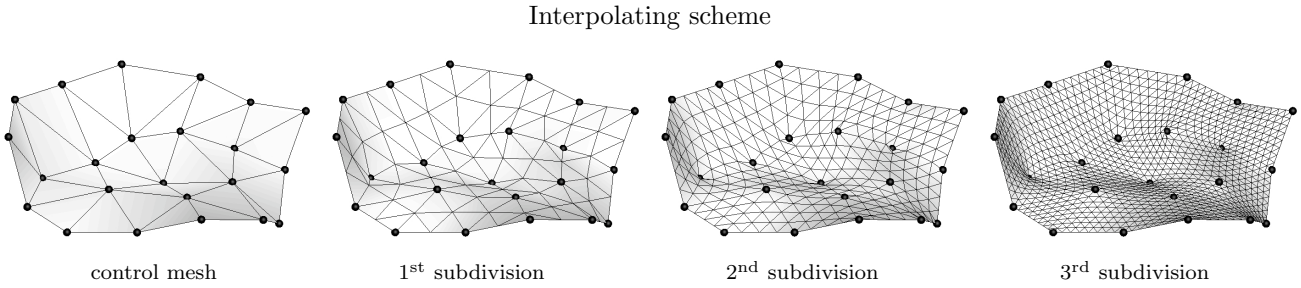

Fig. 4 Interpolating scheme with a control mesh based on the 23 marker coordinates (left) and three levels of subdivision (right). The interpolating algorithm generates surfaces which contain all control points but are not $\mathcal{C}^1$-continuous.

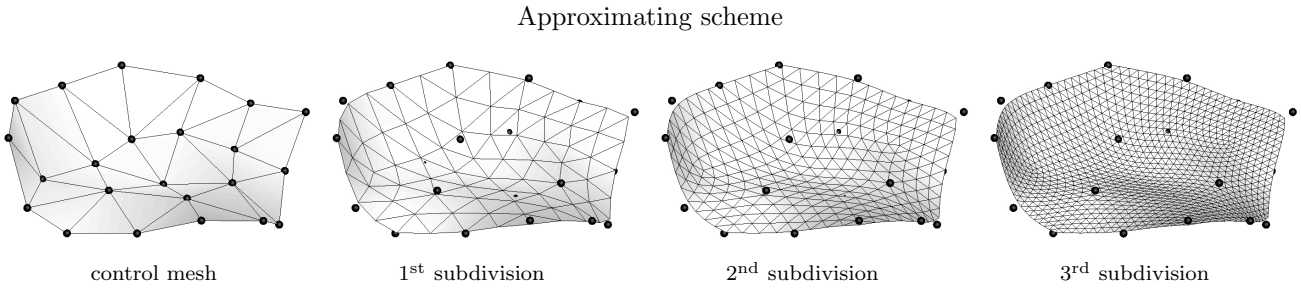

Fig. 5 Approximating scheme with a control mesh based on the 23 marker coordinates (left) and three levels of subdivision (right). The approximating algorithm generates surfaces which are $\mathcal{C}^1$-continuous but only approximate the control points.

norm $||\mathrm{e}||_{\mathrm{L}_2}$ or the average error norm $||\mathrm{e}||_{\mathrm{L}_1}$. In the following examples, we will explore the average error norm

$$||\mathrm{e}||_{\mathrm{L}_1} = \frac{1}{\mathrm{n^{mrk}}} \sum_{i=1}^{\mathrm{n^{mrk}}} |\,\boldsymbol{x}_0^{\mathrm{k}+1} - \boldsymbol{x}_0^1| \tag{5}$$

which characterizes the average distance between the originally measured marker positions $\boldsymbol{x}_0^1$ and their refined position on the subdivision surface of level k.

4 Curvature computation

The key objective of the approximating subdivision algorithm outlined in Section 3.2 is the reconstruction of a sufficiently smooth leaflet surface that allows for curvature tensor field evaluation. At the end of the $\mathrm{k^{th}}$ subdivision, our database contains the nodal coordinates and the connectivity of each triangle on the approximated surface. The curvature field within each triangle T is computed based on the coordinates of its own nodes and those of its immediate neighboring triangles, see Fig. 7. A regular patch consists of twelve nodes with nodal coordinates $\boldsymbol{x}_I$ for $I = 1, .., 12$. The local parametrization of the limit surface can be expressed in terms of quartic box-spline shape functions

$$\boldsymbol{x}(\theta^1, \theta^2) = \sum_{I=1}^{12} N_I(\theta^1, \theta^2)\, \boldsymbol{x}_I \tag{6}$$

where (θ^1, θ^2) are the barycentric coordinates of the master triangle $T = (\theta^1, \theta^2)$ with $\theta^{1,2} \in [0, 1]$ and $\theta^1 + \theta^2 \leq 1$, see Fig. 8. For a regular twelve node patch, the box-spline shape functions are given in [4]. Irregular triangles with nodal valences different from six require special treatment. These irregular patches have to be locally refined one-step further to obtain regular subpatches on which the parametrization (6) can be applied.

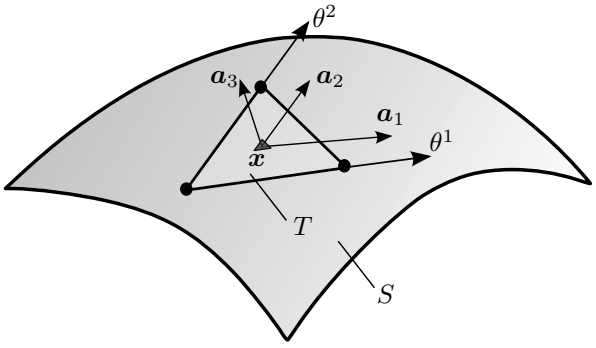

Fig. 8 Surface base vectors $\boldsymbol{a}_1$, $\boldsymbol{a}_2$, the surface normal $\boldsymbol{a}_3$ at the integration point $\boldsymbol{x}$ of an element T on the surface S. The local curvilinear coordinates θ_1, θ_2 are assumed to be identical to the barycentric coordinates of an element.

Having the position vectors $\boldsymbol{x}$ at hand, we can determine the covariant base vectors $\boldsymbol{a}_\alpha$ as

$$\boldsymbol{a}_\alpha(\theta^1, \theta^2) = \sum_{I=1}^{12} N_{I,\alpha}(\theta^1, \theta^2)\, \boldsymbol{x}_I \quad \text{for} \quad \alpha = 1, 2 \tag{7}$$

where $N_{I,\alpha} := \partial N_I / \partial \theta^\alpha$. The normalized vector product of base vectors yields the unit surface normal $\boldsymbol{a}_3$.

$$\boldsymbol{a}_3(\theta^1, \theta^2) := \frac{\boldsymbol{a}_1 \times \boldsymbol{a}_2}{|\boldsymbol{a}_1 \times \boldsymbol{a}_2|} \tag{8}$$

The key quantity describing the local curvature characteristics of a surface is the second fundamental form [12],

$$\boldsymbol{B} = B_{\alpha\beta}\, \boldsymbol{a}^\alpha \otimes \boldsymbol{a}^\beta \quad \text{where} \quad B_{\alpha\beta} := \boldsymbol{a}_{\alpha,\beta} \cdot \boldsymbol{a}_3 \tag{9}$$

with $\boldsymbol{a}_{\alpha,\beta} := \partial \boldsymbol{a}_\alpha / \partial \theta^\beta$. Due to the definition (8) the covariant base vectors $\boldsymbol{a}_\alpha$ are orthogonal to the surface normal $\boldsymbol{a}_3$, see Fig. 8. Hence, the identity $B_{\alpha\beta} = \boldsymbol{a}_{\alpha,\beta} \cdot \boldsymbol{a}_3 = -\boldsymbol{a}_\alpha \cdot \boldsymbol{a}_{3,\beta}$ holds, and so does the equality $B_{\alpha\beta} d\theta^\alpha d\theta^\beta = -\, d\boldsymbol{x} \cdot d\boldsymbol{a}_3$. The latter statement clearly illustrates the geometrical interpretation of the coefficients $B_{\alpha\beta}$. Recall that the contra-variant base vectors $\boldsymbol{a}^\alpha$ are related to the covariant base vectors $\boldsymbol{a}_\beta$ through the inverse of the local surface metric $g^{\alpha\beta}$.

$$\boldsymbol{a}^\alpha := g^{\alpha\beta} \boldsymbol{a}_\beta \tag{10}$$

The symmetric, positive definite surface metric $g_{\alpha\beta}$ and its inverse $g^{\alpha\beta}$ are defined as follows.

$$\begin{aligned} g_{\alpha\beta} &:= \boldsymbol{a}_\alpha \cdot \boldsymbol{a}_\beta \\ g^{\alpha\beta} &:= \boldsymbol{a}^\alpha \cdot \boldsymbol{a}^\beta = (g_{\alpha\beta})^{-1} \end{aligned} \tag{11}$$

The surface metric $g_{\alpha\beta}$, also referred to as the first fundamental form, is another key quantity required to evaluate length measures. In light of the definitions given above, it can readily be shown that contra- and covariant bases are orthogonal $\boldsymbol{a}_\alpha \cdot \boldsymbol{a}^\beta = \delta_\alpha^\beta$ with δ_α^β denoting the Kronecker delta.

The principal curvatures κ at point $\boldsymbol{x}$ on the surface S, Fig. 8, satisfy the principal value problem of the second fundamental form,

$$\boldsymbol{B} \cdot \boldsymbol{n} = \kappa\, \boldsymbol{g} \cdot \boldsymbol{n} \quad \text{or} \quad B_{\alpha\beta} n^\beta = \kappa\, g_{\alpha\beta} n^\beta \tag{12}$$

where $\boldsymbol{n}$ are the corresponding contravariant principal directions. Non-trivial solutions of (12) are obtained for $\det(B_{\alpha\beta} - \kappa\, g_{\alpha\beta}) = 0$ leading to the characteristic equation of the principal curvature problem.

$$\kappa^2 - I_B\, \kappa + II_B = 0 \tag{13}$$

Its coefficients I_B and II_B

$$\begin{aligned} I_B &:= \mathrm{tr}(\boldsymbol{B}) = B_{\alpha\beta}\, g^{\alpha\beta} = \kappa_1 + \kappa_2 \\ II_B &:= \det(\boldsymbol{B}) = \det(B_{\alpha\beta}) / \det(g_{\alpha\beta}) = \kappa_1 \kappa_2 \end{aligned} \tag{14}$$

are the first and the second principal invariants of the second fundamental form $\boldsymbol{B}$. Since $\boldsymbol{B}$ is symmetric, the principal curvatures κ_1, κ_2 are real-valued and the corresponding principal directions $\boldsymbol{n}_1, \boldsymbol{n}_2$ are orthogonal. The principal curvatures $\kappa_{1,2}$ can be determined as the roots of the characteristic equation (13).

$$\kappa_{1,2} = \tfrac{1}{2}\, [\, I_B \pm \sqrt{I_B^2 - 4\, II_B}\,] \tag{15}$$

Next to the principal curvatures $\kappa_{1,2}$, the mean curvature κ^{mean} and the Gaussian curvature κ^{gauss} are commonly employed in the literature to characterize a curvature distribution. In the forthcoming subsections, we introduce the definitions of these curvature measures, illustrate their features in terms of contour plot representations, and discuss their physical interpretation. To this end, we evaluate the second fundamental form $\boldsymbol{B}$ at the barycenter of each triangle $\theta^1 = \theta^2 = 1/3$ using the isoparametric box-spline parametrization (6).

4.1 Mean curvature

The mean curvature is defined as the arithmetic mean of the principal curvatures

$$\kappa^{\mathrm{mean}} := \tfrac{1}{2}\, [\, \kappa_1 + \kappa_2\,] \tag{16}$$

which is equivalent to $\kappa^{\mathrm{mean}} = \frac{1}{2} I_B = \frac{1}{2} \mathrm{tr}(\boldsymbol{B})$ according to $(14)_1$. A surface for which the mean curvature κ^{mean} vanishes at every point is called a minimal surface. It can be shown that the minimal part of a surface with $\kappa^{\mathrm{mean}} = 0$, bounded by a closed curve Γ, possesses the

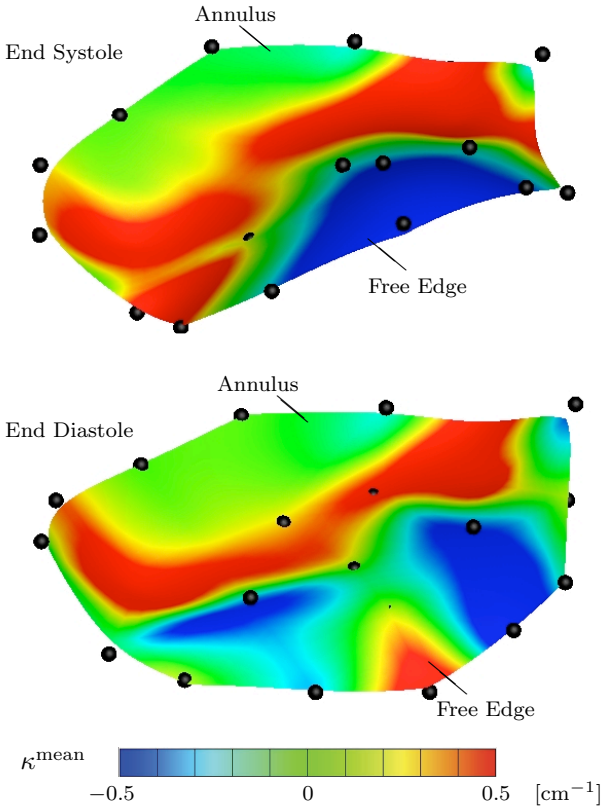

Fig. 9 Mean curvature κ^{mean} at end systole (top) and at end diastole (bottom) for third subdivision with 1017 nodes.

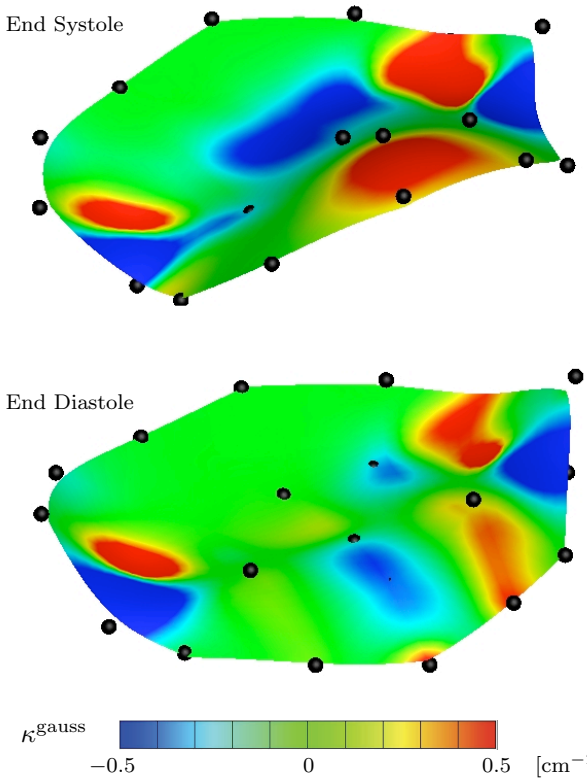

Fig. 10 Gaussian curvature κ^{gauss} at end systole (top) and at end diastole (bottom) for third subdivision with 1017 nodes.

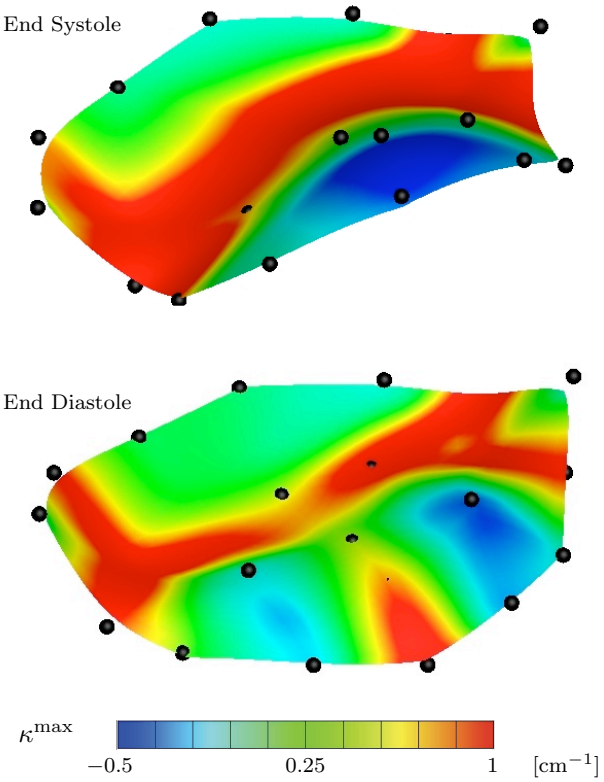

Fig. 11 Maximum principal curvature κ^{max} at end systole (top) and at end diastole (bottom) for third subdivision with 1017 nodes.

smallest area compared to any other part of the surface bounded by the same curve Γ, see [12], p.244. The contours of κ^{mean} in Fig. 9 illustrate the distribution of the mean curvature field over the anterior leaflet at end diastole and at end systole for the third subdivision level with 1017 nodes.

4.2 Gaussian curvature

Another widely used curvature measure is the Gaussian curvature that is defined by the product of principal curvatures.

$$\kappa^{\text{gauss}} := \kappa_1 \kappa_2 \tag{17}$$

It can also be expressed in terms of the second invariant $\kappa^{\text{gauss}} = II_B = \det(\boldsymbol{B})$, see $(14)_2$. The sign of the local Gaussian curvature is used to classify the shape of a surface in the neighborhood of a point $\boldsymbol{x}$. Surface points with positive $\kappa^{\text{gauss}} > 0$ are called *elliptic*, points with negative $\kappa^{\text{gauss}} < 0$ are called *hyperbolic* or saddle points, and points with vanishing $\kappa^{\text{gauss}} = 0$ are referred to as *parabolic*. The contours of the Gaussian curvature κ^{gauss} over the leaflet at end diastole and at end systole are depicted in Fig. 10. The chosen color code clearly demonstrates the elliptic and hyperbolic domains on the leaflet. Although the Gaussian curvature has been used previously to illustrate the surface characteristics of the leaflet [23, 24], it does not readily reflect the leaflet curvature observed on echocardiography. A typical example is an elliptic point with positive $\kappa^{\text{gauss}} > 0$, which can be obtained either for $\kappa_1 > 0$ and $\kappa_2 > 0$ or for $\kappa_1 < 0$ and $\kappa_2 < 0$. Accordingly, convex or concave areas can be assigned the same color code.

4.3 Maximum principal curvature

To make curvature interpretation readily accessible and distinguish convex and concave areas, we propose to use the maximum principal curvature κ^{max}.

$$\kappa^{\text{max}} := \max\{\kappa_1, \kappa_2\} \tag{18}$$

The maximum principal curvature contours over the leaflet at end diastole and at end systole are depicted in Figs. 11 and 12. Compared to the Gaussian curvature contours in Fig. 10, the κ^{max} contours in Fig. 11 transparently distinguish convex and concave regions in the elliptic domains of the leaflet surface at end diastole. However, special attention should be paid to

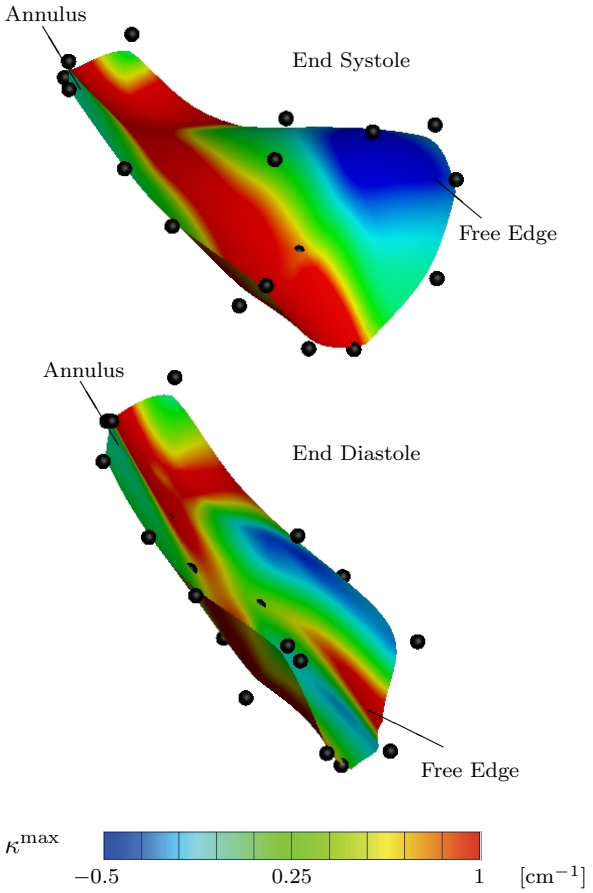

Fig. 12 Maximum principal curvature $\kappa^{\max}$ at end systole (top) and at end diastole (bottom) for third subdivision with 1017 nodes.

the points where the maximum principal curvature is positive. Positive $\kappa^{\max} > 0$ might represent both hyperbolic and convex regions of the surface, and a clear distinction can only be made by analyzing both the Gaussian and the maximum principal curvature contours, see Figs. 10 and 11. Another illustrative feature associated with the maximum principal curvature $\kappa^{\max}$ is the maximum principal direction $\boldsymbol{n}(\kappa^{\max})$ according to the principal value problem in equation (12). Fig. 13 illustrates the maximum principal directions, i.e., the directions with maximum curvature. These are orthogonal to the directions of minimum curvature $\boldsymbol{n}(\kappa^{\min})$ which, in turn, might be correlated to the preferred microstructural orientations of the leaflet, see, e.g., [10,16], for a discussion on leaflet anisotropy, histological staining, and a conceptual model of the leaflet microstructure, respectively.

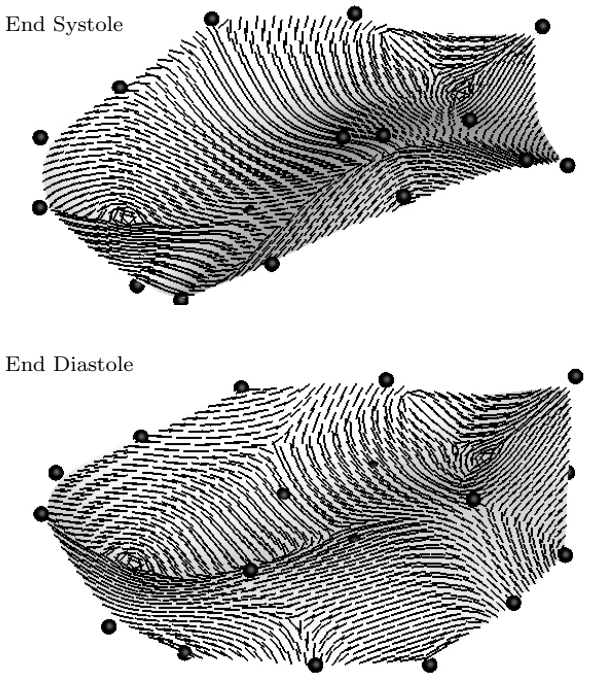

Fig. 13 Maximum principal directions at end systole (top) and at end diastole (bottom) for third subdivision with 1017 nodes.

4.4 Circumferential and radial curvatures

Apart from the curvature measures considered above, we now consider the projection of the second fundamental form $\boldsymbol{B}$ on the circumferential and radial axes of the leaflet at end diastole. For this purpose, we introduce the circumferential κ^{cc} and radial κ^{rr} curvatures

$$\kappa^{\mathrm{cc}} := \boldsymbol{n}^c \cdot \boldsymbol{B} \cdot \boldsymbol{n}^c \quad \text{and} \quad \kappa^{\mathrm{rr}} := \boldsymbol{n}^r \cdot \boldsymbol{B} \cdot \boldsymbol{n}^r \tag{19}$$

where the vectors $\boldsymbol{n}^c$ and $\boldsymbol{n}^r$ denote the unit vectors in the circumferential and radial directions, shown in Fig. 14. Contour plots of these curvature measures are depicted in Figs. 14 and 15, separately. Apparently, the contour plots in these figures partially resemble the $\kappa^{\max}$ distribution, Fig.11, at points where the principal maximum curvature directions, Fig. 13, become nearly parallel to the circumferential and radial directions. Overall, we feel that if we were to pick a single curvature contour plot, the maximum principal curvature $\kappa^{\max}$, Fig. 11, may give the best picture of the leaflet shape. In the following examples, for the sake of completeness, we utilize the circumferential and radial curvature plots besides the maximum principal curvature distribution to characterize ring-induced changes in leaflet kinematics.

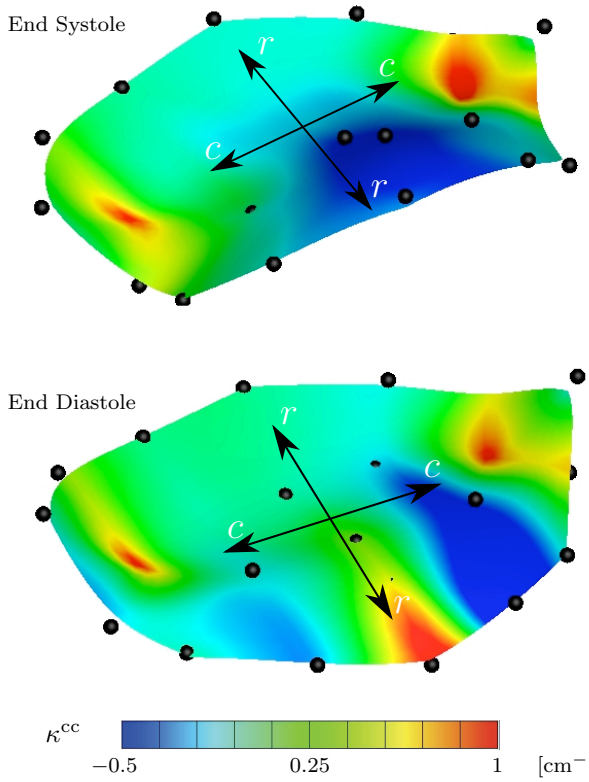

Fig. 14 Circumferential curvature κ^{cc} at end systole (top) and at end diastole (bottom) for third subdivision with 1017 nodes.

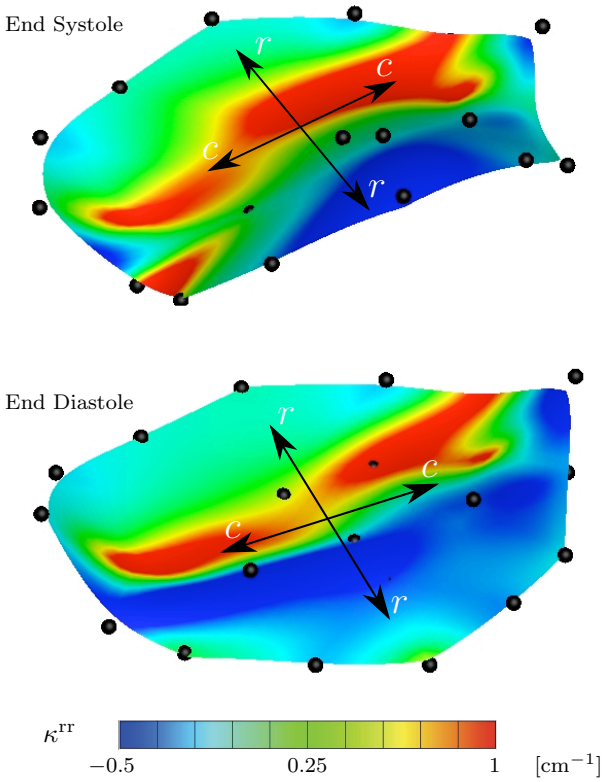

Fig. 15 Radial curvature κ^{rr} at end systole (top) and at end diastole (bottom) for third subdivision with 1017 nodes.

5 Example: Ring-induced kinematic changes

In this section, we explore the impact of annuloplasty rings on mitral leaflet kinematics. In particular, we compare the leaflet surface area and curvature after the insertion of a true-sized 28 mm Edwards GeoForm® ring with the baseline leaflet kinematics without ring. For the acquired data sets of 23 control points at a resolution of 16.6ms, we perform the approximating subdivision up to third level and calculate the total surface area and curvature over a representative cardiac cycle for ring on and ring off, respectively. We focus in particular on three representative configurations of the mitral leaflet that correspond to maximum opening (MO), end diastole (ED), and end systole (ES) as indicated in the left ventricular pressure vs. time curve in Fig. 16. Maximum opening is defined as the maximum distance between the central anterior and posterior leaflet edge markers. End diastole and end systole are identified as the peak R-wave on the EKG and as the time frame preceding the maximum negative pressure gradient, respectively.

5.1 Approximation error of subdivision surface scheme

We begin our analysis by quantifying the approximation error that provides information about the average distance of the original marker positions from the final

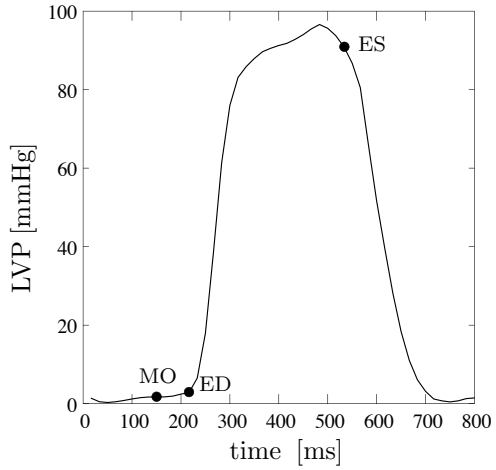

Fig. 16 Evolution of left ventricular pressure (LVP) during a representative cardiac cycle. Filled circles indicate stages of maximum opening (MO), end diastole (ED) and end systole (ES).

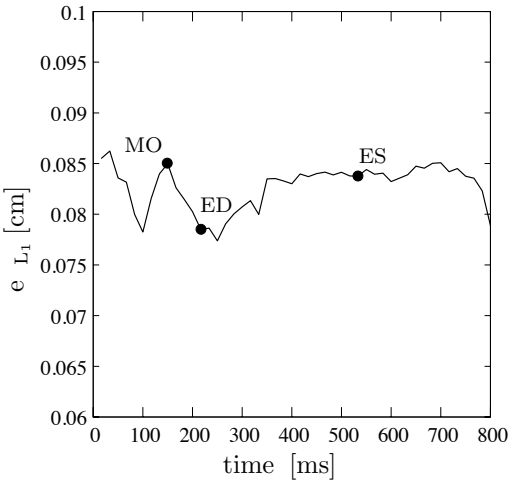

Fig. 17 Evolution of approximation error e_{L_1} during a representative cardiac cycle. Filled circles indicate stages of maximum opening (MO), end diastole (ED) and end systole (ES).

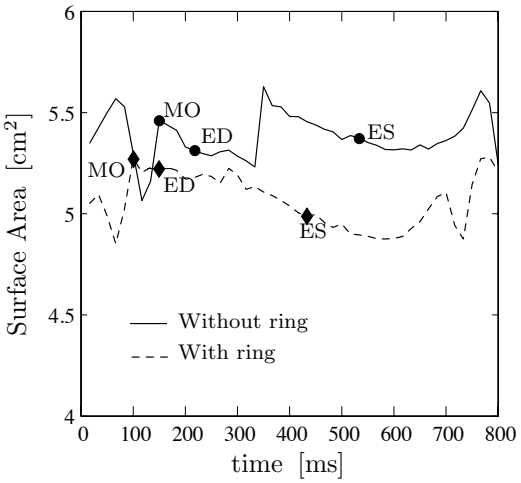

Fig. 18 Evolution of anterior mitral leaflet surface area during a representative cardiac cycle. Filled circles indicate stages of maximum opening (MO), end diastole (ED) and end systole (ES).

subdivision surface. In Fig. 17, we illustrate the temporal evolution of the average approximation error e_{L_1} according to equation (5) for the third level subdivision of a representative leaflet without ring. The maximum average approximation error $e_{L_1} = 0\,0862$ cm occurs in early stages of the cardiac cycle when the valve is open. Given that the mean circumferential dimension of an ovine mitral leaflet is approximately 4 cm, the average error of the approximating third subdivision surface is on the order of 2.3% with respect to the mean circumferential dimension. The average approximation error e_{L_1} is approximately on the order of the digitalization error $e^{dig} = 0\,01 \pm 0\,03$ cm of the videofluoroscopic marker technique [8]. We thus conclude that the average error of the approximating subdivision algorithm lies within a tolerable range.

5.2 Effect of annuloplasty ring on leaflet surface area

The temporal evolution of the surface area of the anterior mitral leaflet with ring and without ring is depicted in Fig. 18. The kinematic constraint imposed by the implanted ring initiates a surface area reduction of approximately 0.25 cm^2. The most significant reduction in surface area occurs at end systole when the area ratio of the leaflet with ring to the leaflet without ring is 93%. This ratio becomes 97% at maximum opening and 98% at end diastole. The observed ring-induced area surface reduction might become even more pronounced in real clinical applications in which down-sized rather than true-sized rings are applied to restore valvular function.

5.3 Effect of annuloplasty ring on leaflet curvature

The impact of annuloplasty ring implantation on the maximum principal curvature, and on the circumferential and radial curvatures is illustrated in Figs. 19, 20 and 21, respectively. The top row in each of these figures depicts the curvature at maximum opening (left), end diastole (middle), and end systole (right) for the leaflet with ring. The bottom rows illustrate the corresponding baseline values for the same leaflet without ring. The comparison of the different curvature contours for the anterior leaflet with and without ring suggests that the true-sized 28 mm Edwards GeoForm® ring has a small influence on the overall curvature distribution on the anterior leaflet. The sequence of snapshots clearly documents the tremendous shape changes of the leaflet during the cardiac cycle. The displayed stages of maximum opening, end diastole, and end systole mimic the underlying blood flow and chord anatomy. Maximum opening manifests itself in a T-channel-shaped convex domain guiding blood flow from the left atrium to left ventricle, shown in red in Fig. 19 (left). The slight increase in left ventricular pressure generates a slightly modified curvature pattern at end diastole. This pressure-induced curvature change is more pronounced for the leaflet without ring Figs. 19 21 (bottom row, middle) than for the leaflet with ring Figs. 19 21 (top row, middle). At end systole, the leaflet adapts to the significantly higher pressure by changing its curvature contours from T-channel-shaped to funnel-shaped, see also Fig.12. The maximum curvature is now aligned with the circumferential direction rather than with the radial direction as it was at end diastole. This characteristic funnel shape

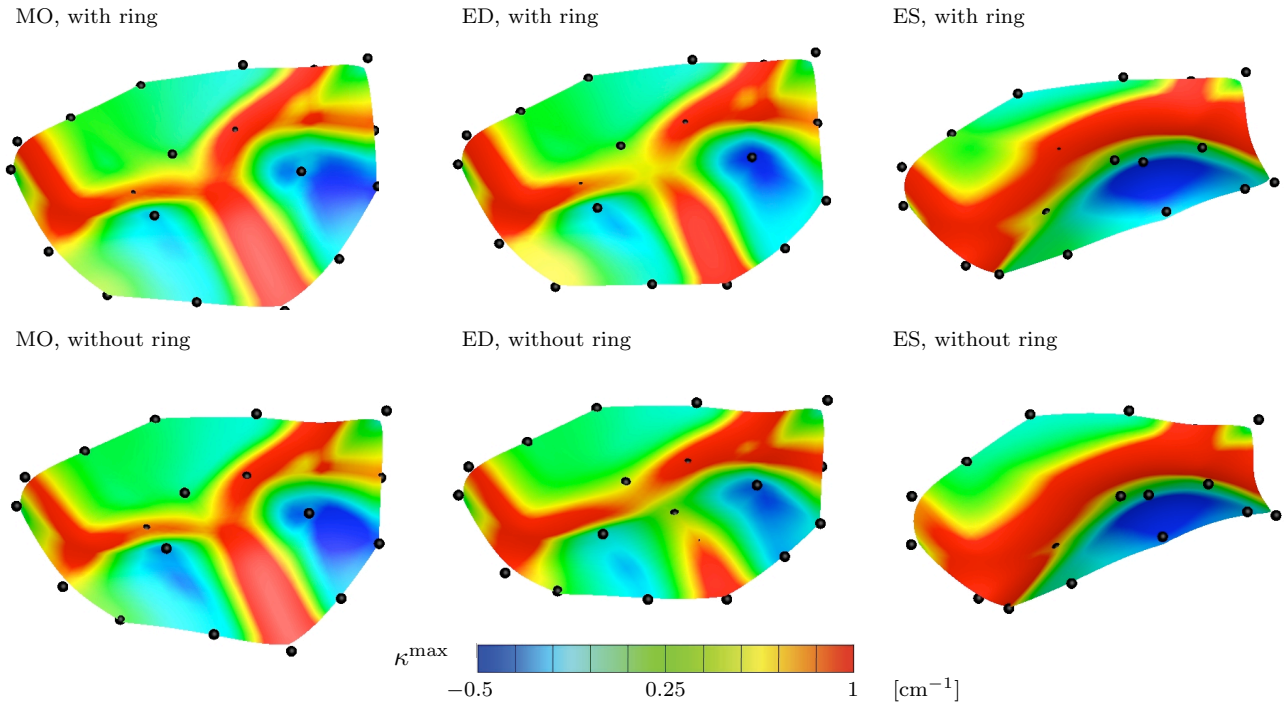

Fig. 19 Maximum principal leaflet curvature at maximum opening (left), end diastole (middle), and end systole (right) with ring (top row) and without ring (bottom row) for third subdivision with 1017 nodes.

at end systole shown in red in Fig. 19 (right) is believed to guide the blood flow underneath the leaflet, from the left ventricle to aorta. Overall, we conclude that ring-induced curvature changes for this particular animal are less pronounced than surface area changes.

6 Discussion

Annuloplasty ring implantation is a common surgical treatment to repair a leaking valve. The shape and size of the ring have been postulated to play a major role in long-term repair durability. Accordingly, annuloplasty rings come in different sizes, shapes, and stiffnesses. To date, the appropriate ring choice is mainly based on the surgeon's experience, and is thus purely empirical. Although it is intuitive that ring size and shape might influences leaflet geometry there is no quantitative evidence showing how leaflet kinematics are affected by ring implantation.

The goal of this study was to create a virtual test environment to classify mitral annular rings based on their effect on leaflet curvature. We acquired four-dimensional mitral leaflet coordinates using a specific videofluoroscopic marker technique that allowed us to study leaflet dynamics with and without ring in the same animal. Since curvature calculations require a non-standard $\mathcal{C}^1$-continuous surface representation, we explored smooth surface generation algorithms which had originally been developed for computer graphics applications. Amongst different surface representation schemes, we chose a triangular approximating scheme capable of generating smooth $\mathcal{C}^1$-continuous surfaces from a set of control points. On patches of neighboring triangles, we interpolated the curvature tensor for each triangle, and assembled the elementwise curvature interpolation to the global curvature field for the entire leaflet. From the resulting second order curvature tensor field, we extracted and compared different scalar-valued curvature measures. We concluded that the maximum principal curvature visualizes leaflet dynamics most illustratively. To demonstrate the features of the proposed approach, we compared maximum principal curvatures in an ovine model with and without ring at three characteristic points in the cardiac cycle. For the ovine model considered in this study, we found that the implantation of a true-sized GeoForm® ring had rather small effects on curvature profiles of the anterior leaflet of the particular animal under investigation.

The proposed methodology offers many advantages with respect to other classification schemes proposed in the literature: (i) In contrast to leaflet stress calculations, the proposed leaflet curvature calculation uses exclusively raw data. It does not imply assumptions about constitutive equations, boundary conditions, and forces acting on the mitral valve apparatus. (ii) In con-

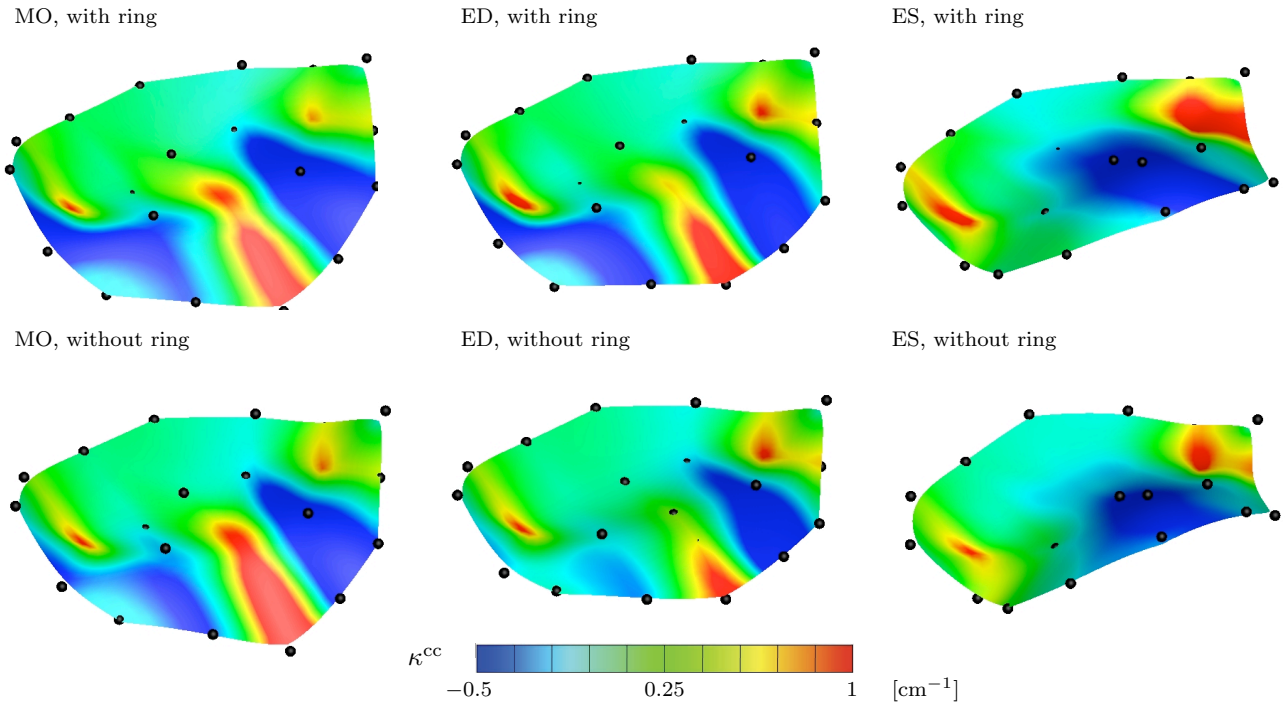

Fig. 20 Circumferential leaflet curvature at maximum opening (left), end diastole (middle), and end systole (right) with ring (top row) and without ring (bottom row) for third subdivision with 1017 nodes. The circumferential direction $\boldsymbol{n}^c$ corresponding to the end systolic and end diastolic configurations is depicted in Fig. 14.

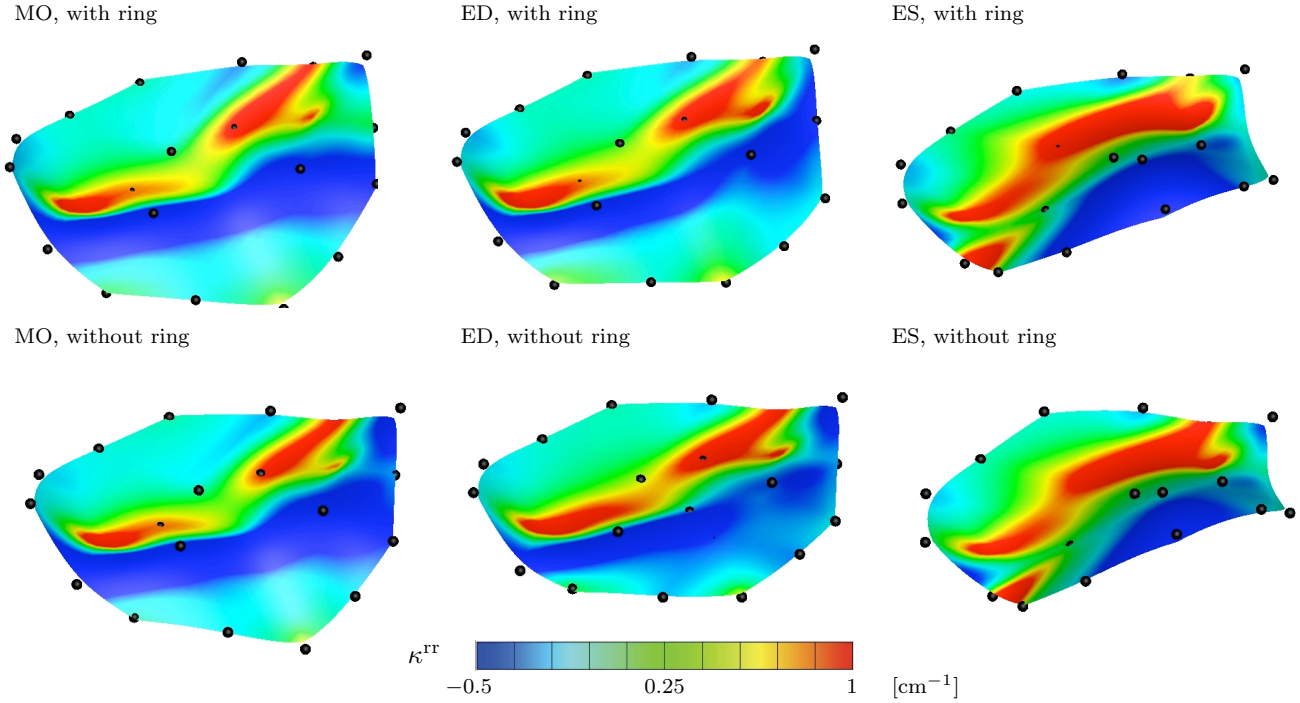

Fig. 21 Radial leaflet curvature at maximum opening (left), end diastole (middle), and end systole (right) with ring (top row) and without ring (bottom row) for third subdivision with 1017 nodes. The radial direction $\boldsymbol{n}^r$ corresponding to the end systolic and end diastolic configurations is depicted in Fig. 15.

trast to echocardiography-based data acquisition, the proposed marker technique is semi-automated. It does not require manual sectioning or manual merging of two-dimensional slices, and is thus less likely to generate errors. (iii) The proposed technique enables us to study curvature with and without ring in the same animal and quantitatively compare curvature changes. (iv) The method offers a high spatial and temporal resolution. This allows us to answer where and when annuloplasty rings affect leaflet curvature most, and how ring geometry could potentially be improved. (v) The underlying smooth surface generations follow well-defined schemes common in computer graphics. They are easily reproducible, and allow for a quantitative assessment of the approximation error. (vi) The generic determination of the curvature tensor field allows us to access different curvature measures, e.g., mean curvature, Gaussian curvature, and maximum principal curvature, and identify the one that is most useful for the current application. The disadvantage of the proposed approach is that it is inherently invasive and based on ovine data. The suggested subdivision surface and curvature calculation, however, is fairly generic and can easily be adapted to control points generated from any other data source, e.g., from echocardiography.

This manuscript has demonstrated the potential of combined experimental/computational approaches to quantify ring-induced curvature changes in the anterior mitral leaflet. Curvature changes in the mitral leaflet have been associated with surgical repair durability. The proposed algorithm is currently being applied to quantify ring-induced leaflet curvature changes in 60 sheep. These animals were divided in five groups of twelve animals each to compare five different ring types. The proposed methodology could potentially serve as a design tool for novel annuloplasty rings with a more physiological shape. The overall goal of this project is to predict curvature changes based on patient-specific mitral valve geometries and identify the optimal ring shape and size on a patient-specific individual basis. This must, of course, be based on non-invasive image modalities that do not require physical markers on the valve.

Acknowledgments

We thank Paul A. Chang, Eleazar P. Briones, and Lauren R. Davis for technical assistance, Maggie Brophy and Sigurd Hartnett for careful marker image digitization, and George T. Daughters, and T.J. and W.S. Hart for extraction of four-dimensional data from marker coordinates. This work was supported in part by the US National Science Foundation grant EFRI-CBE 0735551 to Ellen Kuhl, by US National Institutes of Health grants R01 HL29589 and R01 HL67025 to D. Craig Miller, by the Deutsche Herzstiftung, Frankfurt, Germany, Research Grant S/06/07 to Wolfgang Bothe, by the U.S.- Norway Fulbright Foundation and the Swedish Heart-Lung Foundation to John-Peder Escobar Kvitting, and by the Western States Affiliate American Heart Association Fellowship to Julia C. Swanson.

References

1. Bothe W, Krishnamurthy G, Chang PA, Swanson JC, Briones EP, Davis LR, Itoh A, Ingels NB, Miller CD (2009) Effects of the Geoform® annuloplasty ring on anterior mitral leaflet strains and stresses in the normal ovine heart. submitted for publication.
2. Bornow RO, Carabello BA, Chatterjee K, deLeon AC, Faxon DP, Freed MD, Gaasch WH, Lytle BW, Nischimura RA, O Gara PT, O Rourke RA, Otto CM, Shah PM, Shanewise JS (2006) ACC/AHA 2006 Guidelines for the management of patients with valvular heart disease. Circulation 114: E84-E231.
3. Catmull E, Clark J (1978) Recursively generated B-spline surfaces on arbitrary topological meshes. Computer Aided Design 10: 350355.
4. Cirak F, Ortiz M, Schroder P (2000) Subdivision surfaces: A new paradigm for thin-shell Finite-element analysis. Int J for Numerical Methods Engineering 47: 20392072.
5. Cirak F, Ortiz M (2001) Fully C^1-conforming subdivision elements for finite deformation thin-shell analysis. Int J Numerical Methods Engineering 51: 813833.
6. Cirak F, Scott MJ, Antonsson EK, Ortiz M, Schroder P (2002) Integrated modeling, finite-element analysis, and engineering design for thin-shell structures using subdivision. Computer Aided Design 34: 137148.
7. Cosgrove D (2004) Review: View from North America s cardiac surgeons. Eur J Cardiothoracic Surgery 26: S27S31.
8. Daughters G, Sanders W, Miller DC, Schwarzkopf A, Mead C, Ingels NB (1989) A comparison of two analytical systems for 3-D reconstruction from biplane videoradiograms. IEEE Computers in Cardiology, 15: 79-82.
9. Doo D, Sabin M (1978) Behavior of recursive division surfaces near extraordinary points. Computer Aided Design 10: 356-360.
10. Itoh A, Krishnamurthy G, Swanson J, Ennis D, Bothe W, Kuhl E, Karlsson M, Davis L, Miller DC, Ingels NB (2009) Active stiffening of mitral valve leaflets in the beating heart. Am J Physiol Heart Circ Physiology 296: H1766-1773.
11. Karlsson MO, Glasson JR, Daughters GT, Komeda M, Foppiano LE, Miller DC, Ingels NB (1998) Mitral valve opening in the ovine heart. Am J Physiology Heart Circularory Physiology 274: H552-H563.
12. Kreyszig E (1991) Differential Geometry. Dover Publications, Inc., New York
13. Krishnamurthy G, Ennis DB, Itoh A, Bothe W, Swanson JC, Karlsson M, Kuhl E, Miller DC, Ingels NB (2008) Material properties of the ovine mitral valve anterior leaflet in vivo from inverse finite element analysis. Am J Physiology Heart Circulatory Physiology 295: H1141-H1149.
14. Krishnamurthy G, Itoh A, Bothe W, Swanson J, Kuhl E, Karlsson M, Miller DC, Ingels NB (2009) Stress-strain behavior of mitral valve leaflets in the beating ovine heart. J Biomechanics, in press.
15. Krishnamurthy G, Itoh A, Swanson J, Bothe W, Karlsson M, Kuhl E, Miller DC, Ingels NB (2009) Regional stiffening of the mitral valve anterior leaflet in the beating ovine heart. J Biomechanics, accepted for publication.
16. Kunzelman KS, Cochran RP (1992) Stress/strain characteristics of porcine mitral valve tissue: Parallel versus perpendicular collagen orientation. J Cardiac Surgery 7: 71-78.

17. Loop C (1987) Smooth subdivision surfaces based on triangles. Masters Thesis, University of Utah, Department of Mathematics.
18. Niczyporuk MA, Miller DC (1991) Automatic tracking and digitization of multiple radiopaque myocardial markers. Comp Biomed Res 24: 129-142.
19. Prot V, Skallerud B, Holzapfel GA (2007) Transversely isotropic membrane shells with application to mitral valve mechanics. Constitutive modelling and finite element implementation. Int J Numerical Methods Engineering 71: 987-1008.
20. Prot V, Haaverstad R, Skallerud B (2009) Finite element analysis of the mitral apparatus: Annulus shape effect and chordal force distribution. Biomech Model Mechanobiol 8: 43-55.
21. Reif U (1995) A unified approach to subdivision algorithms near extraordinary points. Computer Aided Geometric Design 12: 153174.
22. Reif U, Schroder P (2001) Curvature integrability of subdivision surfaces. Advances Computational Mathematics 14: 157-174.
23. Ryan LP, Jackson BM, Hamamoto H, Eperjesi TJ, Plappert TJ, St John-Sutton M, Gorman RC, Gorman JH III (2008) The influence of annuloplasty ring geometry on mitral leaflet curvature. Ann Thoracic Surgery, 86: 749-760.
24. Ryan LP, Jackson BM, Eperjesi TJ, Plappert TJ, St John-Sutton M, Gorman RC, Gormann JH III (2008) A methodology for assessing human mitral leaflet curvature using real-time 3-dimensional echocardiography. J Thoracic Cardiovascular Surgery, 136: 726-734.
25. Sacks MA, Enomoto Y, Graybill JR, Merryman WD, Zeeshan A, Yoganathan AP, Levy RJ, Gorman RC, Gorman JH III (2006) In-vivo dynamic deformation of the mitral valve anterior leaflet. Ann Thorac Surg, 82: 1369-1377.
26. Salgo IS, Gorman JH III, Gorman RC, Jackson BM, Bowen FW, Plappert T, St John Sutton MG, Edmunds LH (2002) Effect of annular shape on leaflet curvature in reducing mitral leaflet stress. Circulation, 106: 711-717.
27. Schroder P (2002) Subdivision as a fundamental building block of digital geometry processing algorithms. J Computational Applied Mathematics 149: 207-219.
28. Umlauf G (2000) Analyzing the characteristic map of triangular subdivision schemes. Constructive Approximation 16: 145-155.
29. Votta E, Maisano F, Bolling SF, Alfieri O, Montevecchi FM, Redaelli A (2007) The Geoform disease-specific annuloplasty system: A finite element study. Ann Thoracic Surgery 84: 92-101.
30. Votta E, Caiani E, Veronesi F, Soncini M, Montevecchi FM, Redaelli A (2008) Mitral valve finite-element modelling from ultrasound data: A pilot study for a new approach to understand mitral function and clinical scenarios. Phil Trans Royal Soc A 366: 3411-3434.
31. Zorin D (2000) A method for analysis of C^1-continuity of subdivision surfaces. SIAM J Numerical Analysis 37: 1677-1708.